

# Bubble lift-off size in forced convective subcooled boiling flow

Rong Situ <sup>a,1</sup>, Takashi Hibiki <sup>a,b</sup>, Mamoru Ishii <sup>a,\*</sup>, Michitsugu Mori <sup>c</sup>

<sup>a</sup> School of Nuclear Engineering, Purdue University, 400 Central Drive, West Lafayette, IN 47907-2017, USA

<sup>b</sup> Research Reactor Institute, Kyoto University, 2 Asashironishi, Kumatori, Sennan, Osaka 590-0494, Japan

<sup>c</sup> R&D Center, Tokyo Electric Power Company, 4-1 Egasaki, Tsurumi, Yokohama, Kanagawa 230-8510, Japan

Received 18 April 2005

Available online 2 September 2005

## Abstract

Forced convective subcooled boiling flow experiments were conducted in a BWR-scaled vertical upward annular channel. Water was used as the testing fluid, and the tests were performed at atmospheric pressure. A high-speed digital video camera was applied to capture the dynamics of the bubble nucleation process. Bubble lift-off diameters were obtained from the images for a total of 91 test conditions. A force balance analysis of a growing bubble was performed to predict the bubble lift-off size. The dimensionless form of the bubble lift-off diameter was formulated to be a function of Jacob number and Prandtl number. The proposed model agreed well with the experimental data within the averaged relative deviation of  $\pm 35.2\%$ .

© 2005 Elsevier Ltd. All rights reserved.

**Keywords:** Bubble lift-off size; Subcooled boiling; Flow visualization; Forced convection

## 1. Introduction

The capability to predict two-phase flow behaviors in forced convective subcooled boiling flow is of considerable interest to boiling water reactor (BWR) safety. Currently, the two-fluid model [1] together with the interfacial area transport equation [2] can potentially offer an advanced and accurate analysis of thermal–hydraulic characteristics for nuclear reactor systems.

Furthermore, to apply the interfacial area transport equation to subcooled boiling conditions, several parameters such as nucleation number density, bubble lift-off size and bubble lift-off frequency are required as the boundary conditions.

The bubble lift-off size, i.e., the bubble size when a bubble detaches from the heater surface, could be different from the bubble departure size, which is the bubble size when a bubble detaches from the nucleation site. The bubble departure phenomena in pool boiling have been studied since 1950s. Zuber [3] found that bubble departure and the flow regimes are similar to the formation of gas bubbles at orifices. According to Zuber [4], three regimes of vapor bubble departure from the nucleation site can be discerned: (1) Laminar regime: when vapor flow rates are very low, bubbles rise at a constant velocity, and do not interact with each other. The bubble

\* Corresponding author. Tel.: +1 765 494 4587; fax: +1 765 494 9570.

E-mail address: [ishii@ecn.purdue.edu](mailto:ishii@ecn.purdue.edu) (M. Ishii).

<sup>1</sup> Present address: School of Aerospace, Mechanical and Manufacturing Engineering, RMIT University, P.O. Box 71, Bundoora, VIC 3083, Australia.

**Nomenclature**

$b$	constant	$u_r$	relative velocity between bubble center of mass and the liquid phase
$C^+$	constant	$V_b$	bubble volume
$C_f$	friction coefficient	$V_f$	volume of virtual added mass
$C_l$	shear lift coefficient	$v_f$	area-averaged liquid velocity
$C_r$	relative velocity coefficient	$v_g$	gas velocity
$C_p$	specific heat at constant pressure	$x$	coordinate
$D_H$	hydraulic equivalent diameter	$z$	axial coordinate
$D_{lo}$	bubble lift-off diameter		
$D_{lo}^*$	dimensionless bubble lift-off diameter		
$D_w$	bubble contact diameter on surface		
$F$	enhance factor on $h_c$ due to the presence of vapor	<i>Greek symbols</i>	
$F_b$	buoyancy force	$\alpha$	thermal diffusivity
$F_d$	drag force	$\Delta T_{sat}$	wall superheat
$F_{du}$	unsteady drag force (growth force)	$\lambda$	friction factor
$F_g$	gravity force	$\mu$	viscosity
$F_p$	pressure force	$\nu$	kinematic viscosity
$F_{qs}$	quasi-steady force	$\theta_a$	advancing contact angle
$F_s$	surface tension force	$\theta_i$	inclination angle
$F_{sl}$	shear lift force	$\theta_r$	receding contact angle
$G$	mass flux	$\rho$	density
$G_s$	dimensionless fluid velocity gradient	$\sigma$	surface tension
$H$	bubble height	$\tau_w$	wall shear stress
$h$	heat transfer coefficient	<i>Subscripts</i>	
$h_{fg}$	heat of vaporization (latent heat)	b	bubble
$Ja$	Jacob number	c	convective
$k$	thermal conductivity	d	departure
$k^+$	constant	e	effective
$n$	constant	f	liquid phase
$Pr$	Prandtl number	fin	liquid at inlet
$q''$	heat flux	g	vapor phase
$Re_b$	bubble Reynolds number	h	hydraulic
$Re_{TP}$	two-phase flow Reynolds number	i	interfacial
$r_b$	bubble radius	in	inlet
$\dot{r}_b$	derivative of bubble radius with respect to time	lo	bubble lift-off
$\ddot{r}_b$	second derivative of bubble radius with respect to time	NB	nucleate boiling
$S$	suppression factor	sat	saturation
$T$	temperature	w	wall
$t$	time	x	x-direction
$t_{lo}$	time of bubble lift-off	y	y-direction
$u_{bx}$	bubble front velocity on x-direction	<i>Superscripts</i>	
$u_l(x)$	liquid velocity profile near wall	*	dimensionless quantities
		+	dimensionless quantities

diameter is almost independent of vapor flow rate, and the bubble departure frequency increases with increasing vapor flow rate. This regime is also referred as the region of static, separated or isolated bubbles. (2) Turbulent regime: when vapor flow rates are intermediate, the bubble departure diameter increases with flow rate while bubble departure frequency remains constant. A bubble inter-

acts and may coalesce with its predecessor above the nucleation site, and the bubble size is non-uniform. This regime is also referred as the region of multiple or interfering bubbles. (3) When vapor flow rates are even higher, a swirling vapor stream is generated at the nucleation site. The vapor jet is similar to a tornado or a waterspout. In our experiments, the bubble departure

phenomena in subcooled boiling condition fall in the laminar and turbulent regimes.

In most of the existing efforts to model the bubble departure size or bubble lift-off size, a force balance analysis of a bubble was carried out at the instant of departure or lift-off. For bubble departure, the force balance along the flow direction was usually considered [5], while for bubble lift-off, the force balance normal to the flow direction was crucial [6,7].

Levy [5] postulated that the point of bubble departure was determined from the force balance on a bubble at its nucleation site and the single-phase liquid turbulent temperature distribution away from the heated wall. In his force balance equation, the buoyancy force and wall shear force was assumed to detach the bubble, while surface tension force was to hold it on the wall. He derived a non-dimensional equation for the bubble distance from the bubble tip to the wall, which is related to bubble departure size. Staub [8] considered several different forces acting on a nucleating bubble, including surface tension, momentum change of the liquid due to the growth of the bubble, liquid inertia force, evaporation vapor thrust force, buoyancy force, and drag force. He then assumed that the surface tension, buoyancy, and drag forces were the dominant forces. In his model, the force balance is analyzed on a layer of hemispherical bubble, while in Levy's model it was made on a spherical bubble. Al-Hayes and Winterton [9] modified the friction term of Levy's model to be a drag force in modeling the bubble departure size. Their bubble departure size model was adopted later in the model of Rogers et al. [10]. The model of Rogers et al. [10] was mainly based on Al-Hayes and Winterton's model [9] with minor modification. They postulated that the friction factor, heat transfer coefficient, velocity profile and temperature profile at the bubble departure point could be determined from the relationships established for a smooth surface, and the bubble shape was assumed to be distorted by buoyancy and drag force. Kandlikar and Stumm [11] divided a bubble into the front and the rear regions as two control volumes, and performed force balance analysis on both volumes. Several forces such as surface tension, buoyancy, drag, pressure difference and momentum changes were taken into account. Zeng et al. [7] studied the forces acting on a bubble in saturated horizontal forced convection boiling. At the point of bubble departure and bubble lift-off, several forces such as surface tension, hydrodynamic pressure force, and contact pressure force were neglected because the bubble contact area on the wall was approximated to be zero. The bubble departure diameter and bubble lift-off diameter were modeled based on the simplified force balance equation.

Literature review shows that bubble departure size at forced convection boiling have been studied extensively. However, only limited research has been performed on the bubble lift-off size in convective boiling, which is

more important to the interfacial area transport equations than the bubble departure size. When bubbles are attached on the heater surface, they are heated from the heating surface, and vaporization takes place at a micro-layer under the bubbles. The heat transfer mechanism at the wall is different from that in the bulk region, which is used in the interfacial area transport equation to control bubble growth or condensation. Thus bubble departure diameter is not appropriate to act as the boundary condition for the interfacial area transport equation.

The purpose of this research is to study the bubble lift-off size in vertical upward forced convective subcooled boiling flow. The investigation will be carried out in both experimental and theoretical aspects.

## 2. Experiment

### 2.1. Experimental facility

An experimental facility has been designed to measure the relevant two-phase parameters necessary for developing constitutive models for the two-fluid model in subcooled boiling flow. The experimental facility is a scaled-down loop from a prototypic BWR based on proper scaling criteria for geometric, hydrodynamic, and thermal similarities [12,13]. The schematic diagram of the flow loop is shown in Fig. 1. The subcooled water

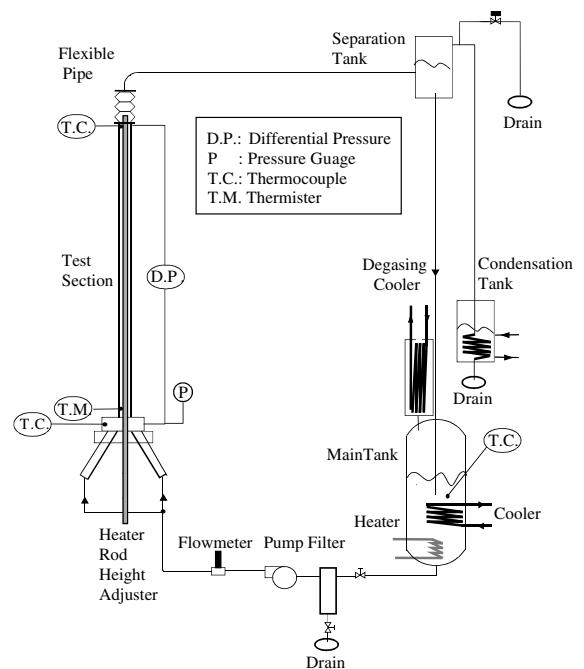


Fig. 1. Schematic diagram of experimental loop.

is held in the main tank. The main tank has a cartridge heater and heat exchanger to control the test-section-inlet subcooling. The water is pumped by a positive displacement pump and divided into four separate lines. Each line runs to a fitting that is connected to the bottom of the test section. The test section is an annulus formed by a clear polycarbonate tube on the outside with an ID of 38.1 mm, and a cartridge heater on the inside with an OD of 19.1 mm. Thus, the hydraulic equivalent diameter,  $D_H$ , is 19.1 mm. The heater has an overall length of 2670 mm with a heated section of 1730 mm in length. The distance between the test section inlet and the heating section inlet is 212 mm. The maximum power of the heater is 20 kW that corresponds to a maximum heat flux of  $0.193 \text{ MW/m}^2$ . At the top of the test section, an expansion joint is installed to accommodate the thermal expansion of the polycarbonate test section. A separation tank is used to separate vapor phase from water. The steam is then condensed, and the water is returned to the main tank. The separation tank is located directly above the main tank. The detailed description of the experimental facility is found in our previous papers [13,14].

## 2.2. Experimental setup of flow visualization

The setup of the flow visualization system [15] is described in Fig. 2. A CCD camera is mounted on the back of a magnification-changeable bellow with a C-mount, and a Micro-NIKKOR 105 mm 1:2.8 lens is mounted in front of the bellow. The camera is placed on a 1-D traverse rail that can be moved forward or backward relative to the test section in a certain range. The 1-D traverse rail is placed on a 2-D traverse system that can be moved vertically (5.0 cm) and laterally

(11.4 cm). This forms a 3-D traverse system. An image box is installed on the test section to minimize the image distortion since the front side of the image box (close to the camera) is filled with water. The side surface of the image box is covered by black paper to avoid any side-light. Two 300 W GE spotlights, supported by adjustable arms, are located behind the image box to provide lighting for the flow visualization.

In preparing for an experiment, the water in the main tank was degassed by heating up the tank for 24 h. Before the measurement, the flow reached steady state, and the inlet temperature and fluid velocity kept constant for 30 min. The high-speed video camera was adjusted to focus on an active nucleation site. In order to capture the very short bubble-growth period, i.e., only a few milliseconds, the camera frame rate was set as high as 5000 frame/s (fps), and the resolution of each image was  $80 \times 120$  pixels, which corresponds to a  $1.3 \times 2.1 \text{ mm}$  window in reality. The distance between adjacent pixels is  $16 \mu\text{m}$ . The shutter speed is  $1/20,000 \text{ s}$ . By adjusting the magnification ratio of the camera, a whole nucleation site along with a certain downstream distance can be covered. For each recording, a total of 13,104 frames of pictures, i.e., 2.6 s images, were taken by the video camera and downloaded to a computer. In general, one recording was made for each flow condition in the current experiments. Fig. 3 shows typical consecutive images of bubble departure and lift-off at the inlet temperature,  $T_{in}$ , of  $90 \text{ }^\circ\text{C}$ , the heat flux,  $q''$ , of  $145 \text{ kW/m}^2$ , the inlet liquid velocity,  $v_{in}$ , of  $0.927 \text{ m/s}$ , and the axial distance between the beginning location of the heated section and a specific nucleation site,  $z_d$ , of  $1.12 \text{ mm}$ . The arrows in the images at the time of 0.2 and 2.0 ms indicate the locations at bubble nucleation site and bubble lift-off, respectively.

A Matlab program has been developed to analyze the digital images and to calculate the bubble diameter when a bubble is attached on the heater rod or in the bulk liquid. The images were calibrated by taking photos of a set of stainless tubes with known diameters. The error caused by the light distortion is significantly reduced by adding the image box. The measurement error of bubble diameter can be estimated as the pixel distance, i.e.,  $16 \mu\text{m}$ .

In the present study, only bubble lift-off diameter is measured because of the following two reasons. The first reason is that the bubble lift-off diameter is more suitable than bubble departure diameter to be used as the boundary condition for the interfacial area transport equation, which is explained earlier. The second reason is the difficulty in defining the instant of bubble departure from the nucleation site. Since the bubble lift-off diameter is not uniform, a number of bubbles are measured and averaged for each flow conditions, typically 50 bubbles for one flow condition, which are statistically enough for the lift-off diameter estimation. Recently,

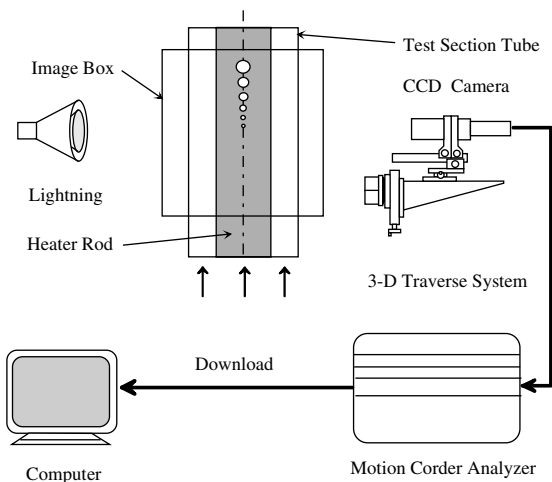


Fig. 2. Schematic diagram of experimental setup of flow visualization.

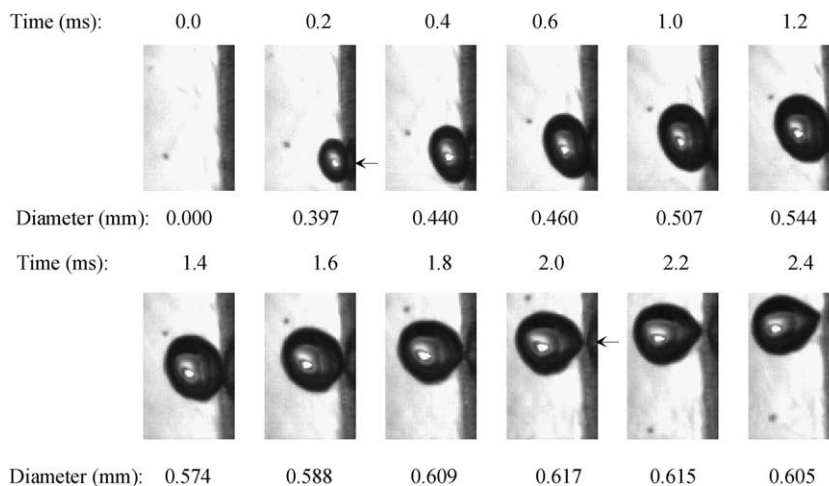


Fig. 3. Typical consecutive images of bubble departure and lift-off.

Hazuku et al. [16] calculated void fraction from bubbly images for bubbly flow in a minipipe. They also found that the measured void fraction converges within  $\pm 3\%$  when the processed image number is higher than 50.

### 2.3. Experimental conditions

Experiments of 91 conditions were performed for the study of the bubble lift-off size through flow visualization. Table 1 lists the experimental parameters for all the conditions. The inlet temperature ranges from 80.0 to 98.5 °C; the inlet velocity varies from 0.487 to 0.939 m/s; and the heat flux changes from 60.7 to 206 kW/m<sup>2</sup>. In the table,  $z_d$  represents the distance between the beginning location of the heated section and a specific nucleation site, where the bubble lift-off diameter,  $D_{lo}$ , are measured. At every steady-state experimental condition, the heater power, inlet water temperature, and inlet water velocity were chosen in such a way that a stable active nucleation site is observed and could be captured by the high-speed video camera.

The inlet temperature was measured by the thermistor probe with interchangeable sensor accuracy of  $\pm 0.1$  °C. The pressure drop cross the test section is measured by Honeywell ST 3000 Smart Transmitter. The combined zero and span inaccuracy for the differential pressure cell is  $\pm 0.4$  % of span. Heat flux and inlet velocity were acquired by a data acquisition system. The measurement accuracies of heat flux, liquid temperature, liquid velocity, pressure, and differential pressure are  $\pm 1\%$ ,  $\pm 0.1$  °C,  $\pm 1\%$ ,  $\pm 1\%$  full-scale reading (55 kPa), and  $\pm 1\%$  full-scale reading (6.9 kPa), respectively.

After the measurement at one flow condition were finished, the next condition was reached either by adjusting the inlet liquid velocity, for example, Tests 1–6, or by

changing the inlet temperature, for instance, Tests 9–13. In Table 1, the adjacent rows with the same  $z_d$  refer to the same nucleation site.

## 3. Results and discussion

### 3.1. Dependence of thermal and flow parameters on bubble lift-off diameter

The averaged bubble lift-off diameters,  $D_{lo}$ , are list in Table 1. The range of lift-off diameter is between 0.15 and 0.61 mm. Fig. 4 shows the measured bubble lift-off diameter against the inlet temperature. The figure indicates that the bubble lift-off diameter increases as the inlet temperature increases. Because nucleation sites are captured at different axial positions, and have different cavity sizes, it is rather difficult to compare the bubble lift-off diameter between the nucleation sites.

Fig. 5 shows the bubble lift-off diameter against the inlet temperature for one nucleation site at  $z_d = 1.13$  m. It suggests that the bubble lift-off diameter increases as the inlet temperature increases. The effect of the heat flux can also be found in this figure. The data indicated by  $\circ$ ,  $\triangle$ , and  $\square$ , have similar inlet fluid velocity but different heat flux. The figure indicates that the solid curve (linear fit of the  $\circ$  data,  $q'' = 202$  kW/m<sup>2</sup>) is higher than the broken curve (linear fit of the  $\triangle$  data, with  $q'' = 146$  kW/m<sup>2</sup>), and the broken curve is higher than the  $\square$  data (with  $q'' = 101$  kW/m<sup>2</sup>). The effect of fluid velocity is suggested by comparing the  $\square$  and  $\nabla$  data. Assuming the dependence of the  $\square$  and  $\nabla$  data on the inlet temperature are similar to the solid and broken curves in the figure, the curve with lower fluid velocity ( $\nabla$ ,  $v_{in} = 0.487$  m/s) would be higher than that with higher inlet fluid velocity ( $\square$ ,  $v_{in} = 0.912$  m/s). Higher

Table 1  
Experimental conditions and measured bubble lift-off diameter

Test	$T_{in}$ (°C)	$q''$ (kW/m <sup>2</sup> )	$v_{fin}$ (m/s)	$z_d$ (m)	$D_{lo}$ (mm)
1	90.0	145	0.927	1.12	0.577
2	90.0	148	0.925	1.12	0.503
3	90.0	136	0.924	1.12	0.433
4	90.0	145	0.921	1.12	0.476
5	90.0	154	0.924	1.12	0.542
6	90.0	158	0.924	1.12	0.497
7	87.6	146	0.926	1.12	0.304
8	91.2	146	0.922	1.12	0.505
9	89.0	143	0.927	1.13	0.350
10	87.6	142	0.929	1.13	0.325
11	90.0	143	0.926	1.13	0.347
12	91.2	142	0.920	1.13	0.384
13	93.0	145	0.919	1.13	0.465
14	80.0	202	0.937	1.13	0.201
15	83.0	202	0.934	1.13	0.302
16	94.0	101	0.912	1.13	0.406
17	85.0	104	0.487	1.13	0.324
18	90.0	142	0.922	0.700	0.275
19	89.0	144	0.926	0.700	0.268
20	91.0	145	0.923	0.700	0.235
21	92.0	146	0.917	0.700	0.287
22	93.5	144	0.919	0.700	0.282
23	80.0	206	0.935	0.700	0.220
24	83.0	202	0.939	0.700	0.224
25	90.0	143	0.926	0.673	0.190
26	89.0	143	0.925	0.673	0.187
27	92.0	143	0.924	0.673	0.226
28	94.0	144	0.915	0.673	0.212
29	94.5	62.0	0.498	0.626	0.287
30	94.0	65.0	0.501	0.626	0.267
31	95.7	62.8	0.498	0.641	0.246
32	94.0	62.4	0.501	0.641	0.224
33	92.6	63.1	0.504	0.641	0.236
34	91.6	62.3	0.503	0.641	0.214
35	93.0	61.5	0.504	0.626	0.211
36	92.0	61.1	0.501	0.626	0.211
37	91.0	61.5	0.507	0.626	0.219
38	90.0	61.9	0.508	0.626	0.186
39	89.0	99.9	0.511	0.626	0.239
40	88.0	100	0.514	0.626	0.225
41	87.0	99.9	0.508	0.626	0.242
42	86.0	99.5	0.508	0.626	0.237
43	85.0	99.4	0.510	0.626	0.220
45	88.0	99.8	0.506	0.655	0.475
46	87.0	101	0.508	0.655	0.447
47	86.0	101	0.507	0.655	0.358
48	85.0	101	0.511	0.655	0.317
49	84.0	107	0.513	0.655	0.270
50	83.0	101	0.511	0.655	0.210
51	88.0	95.0	0.506	0.665	0.434
52	87.0	106	0.510	0.665	0.442
53	86.0	105	0.510	0.665	0.399
54	85.0	98.2	0.509	0.665	0.260
55	84.0	98.2	0.510	0.665	0.223
56	88.0	105	0.504	0.660	0.457
57	87.0	104	0.654	0.660	0.429

Table 1 (continued)

Test	$T_{in}$ (°C)	$q''$ (kW/m <sup>2</sup> )	$v_{fin}$ (m/s)	$z_d$ (m)	$D_{lo}$ (mm)
58	86.0	103	0.508	0.660	0.419
59	85.0	104	0.509	0.660	0.383
60	84.0	105	0.514	0.660	0.314
61	98.5	60.7	0.496	0.668	0.605
62	97.0	62.9	0.497	0.668	0.517
63	95.5	63.3	0.503	0.668	0.413
64	94.0	62.9	0.503	0.668	0.216
65	92.5	63.8	0.509	0.668	0.217
66	96.0	105	0.731	0.677	0.321
67	95.0	99.6	0.752	0.677	0.262
68	96.0	105	0.754	0.677	0.312
69	94.0	95.8	0.755	0.677	0.315
70	92.0	105	0.750	0.677	0.253
71	97.0	105	0.743	0.670	0.334
72	95.0	102	0.744	0.670	0.318
73	93.0	103	0.748	0.670	0.321
74	92.0	103	0.750	0.670	0.230
75	95.0	106	0.749	0.640	0.265
76	93.0	104	0.751	0.640	0.212
77	92.0	104	0.749	0.640	0.177
78	91.0	104	0.753	0.640	0.176
79	89.0	106	0.758	0.640	0.145
80	92.0	142	0.751	0.640	0.311
81	90.0	142	0.752	0.640	0.314
82	88.0	144	0.759	0.640	0.297
83	86.0	144	0.761	0.640	0.321
84	92.0	141	0.751	0.631	0.589
85	90.0	142	0.753	0.631	0.496
86	88.0	142	0.751	0.631	0.418
87	86.0	144	0.757	0.631	0.315
88	92.0	139	0.742	0.570	0.457
89	90.0	142	0.747	0.570	0.490
90	88.0	145	0.751	0.570	0.412
91	86.0	144	0.752	0.570	0.313

inlet temperature, higher heat flux, or lower fluid velocity would result in higher wall temperature at the nucleation site, and thus higher bubble lift-off diameter.

### 3.2. Modeling of bubble lift-off diameter

#### 3.2.1. Basic concept of bubble lift-off

An active nucleation site in upward forced convection subcooled boiling is shown schematically in Fig. 6. At first, a bubble is nucleated at the nucleation site, and then it gradually grows. After reaching a certain size, it departs from the nucleation site. After departure, the bubble may slide on the heater surface. Then, vaporization occurs at the inner surface of the bubble, while condensation takes place at the outer surface if the tip of the bubbles is out of the superheated layer. Whether the bubble will eventually grow or be condensed is governed by the overall effect of these two processes. However, at some distance downstream of the

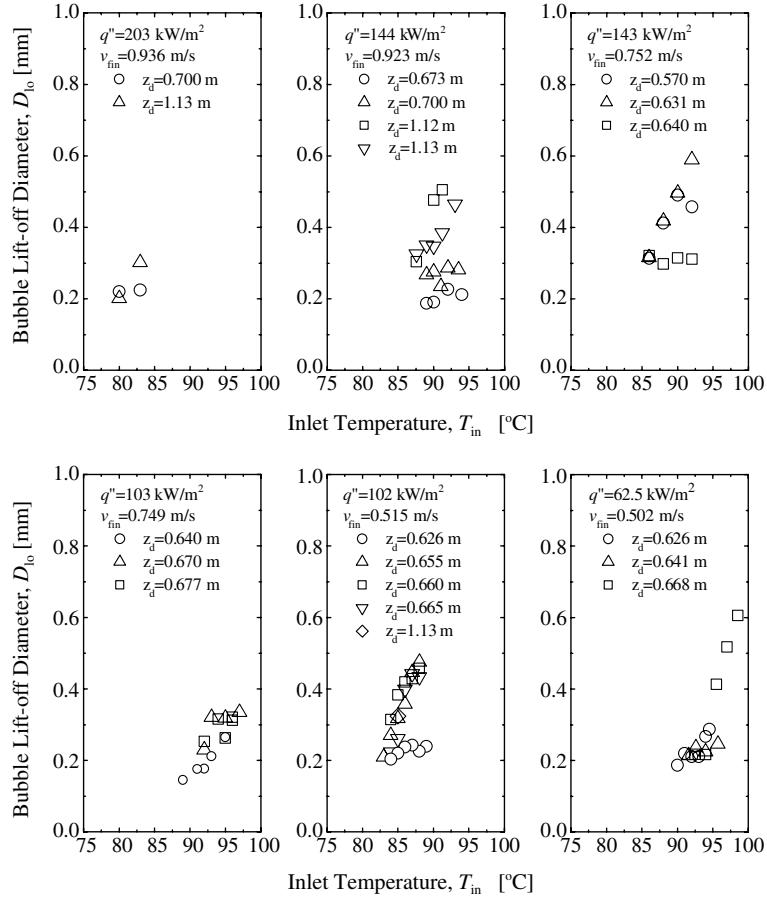


Fig. 4. Dependence of bubble lift-off diameter on inlet temperature.

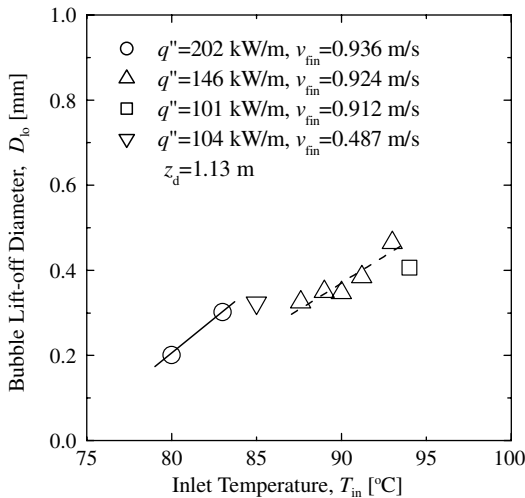


Fig. 5. Dependence of bubble lift-off diameter on inlet temperature at  $z_d = 1.13 \text{ m}$ .

nucleation site, the bubble eventually lifts off from the heater surface.

### 3.2.2. Balance of forces acting on bubble at nucleation site

The forces acting on a bubble at its nucleation site are schematically shown in Fig. 7. The forces can be projected into  $x$ - and  $y$ -directions and are given as

$$\sum F_x = F_{sx} + F_{dux} + F_{sl} = \rho_g V_b \frac{dv_{gx}}{dt} \quad (1)$$

and

$$\sum F_y = F_{sy} + F_{duy} + F_p + F_g + F_{qs} = \rho_g V_b \frac{dv_{gy}}{dt}, \quad (2)$$

where  $F_x$ ,  $F_{sx}$ ,  $F_{dux}$ ,  $F_{sl}$ ,  $\rho_g$ ,  $V_b$ ,  $v_{gx}$ ,  $t$ ,  $F_y$ ,  $F_{sy}$ ,  $F_{duy}$ ,  $F_p$ ,  $F_g$ ,  $F_{qs}$  and  $v_{gy}$  are the force at  $x$ -direction, the surface tension force at  $x$ -direction, the unsteady drag force (growth force) at  $x$ -direction, the shear lift force, vapor density, bubble volume, bubble velocity at  $x$ -direction, time, the force at  $y$ -direction, the surface tension force at  $y$ -direction, the unsteady drag force at  $y$ -direction, the pressure force, the gravity force, the

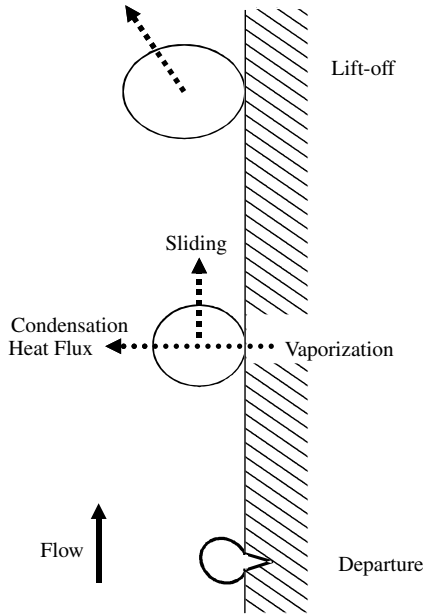


Fig. 6. Schematic diagram of bubble nucleation phenomenon.

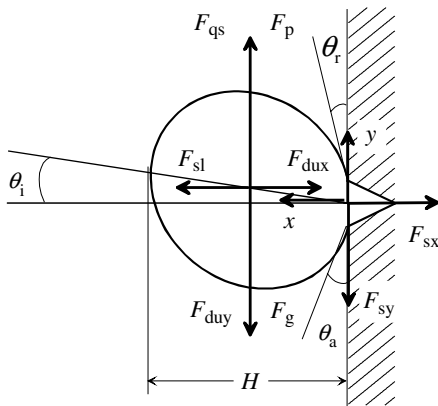


Fig. 7. Force balance of a vapor bubble at a nucleation site.

quasi-steady force, and the bubble velocity at  $y$ -direction respectively.

In Fig. 7, there is an inclination angle,  $\theta_i$  ( $i = a$ : advancing contact angle;  $r$ : receding contact angle) between the line from nucleation site to the bubble center and  $x$ -direction. The surface tension force and unsteady drag forces are projected into  $x$ - and  $y$ -directions as well.

**3.2.2.1. Surface tension force.** The surface tension forces at  $x$ - and  $y$ -directions were given by Klausner et al. [6] as

$$F_{sx} = -D_w \sigma \frac{\pi}{\theta_a - \theta_r} (\cos \theta_r - \cos \theta_a) \quad (3)$$

and

$$F_{sy} = -1.25 D_w \sigma \frac{\pi(\theta_r - \theta_a)}{\pi^2 - (\theta_r - \theta_a)^2} (\sin \theta_a + \sin \theta_r), \quad (4)$$

where  $D_w$ ,  $\sigma$ ,  $\theta_a$ , and  $\theta_r$  are the bubble contact diameter on the heater surface, surface tension, the advancing contact angle, and the receding contact angle, as shown in Fig. 7.

**3.2.2.2. Growth force.** The growth force is also called unsteady drag force. For a spherical bubble attached to a wall, the virtual added mass,  $V_f$ , is given by Chen [17] as

$$V_f = \frac{11}{12} \pi r_b^3, \quad (5)$$

where  $r_b$  is bubble radius. The growth force can be deemed as the inertial force of this added mass as

$$F_{du} = \frac{d(\rho_f V_f u_{bx})}{dt} = \rho_f \left( V_f \frac{d^2 H}{dt^2} + \frac{dH}{dt} \frac{dV_f}{dt} \right), \quad (6)$$

where  $\rho_f$  is liquid density,  $H$  is the bubble height measured from the wall, and  $u_{bx}$  is the bubble front velocity on  $x$ -direction  $u_{bx} = dH/dt$ . For spherical bubble,  $H$  is the bubble diameter. Thus,  $u_{bx} = 2dr_b/dt$ . Thus from Eqs. (5) and (6), the growth force is expressed as

$$F_{du} = -\rho_f \pi r_b^2 \left( \frac{11}{2} \dot{r}_b^2 + \frac{11}{6} r_b \ddot{r}_b \right), \quad (7)$$

where  $\dot{r}_b$  is the derivative of the bubble radius with respect to time,  $\ddot{r}_b$  is the second derivative of the bubble radius with respect to time.

The growth force in  $x$ - and  $y$ -directions can be expressed by considering the inclination angle  $\theta_i$  as

$$F_{dux} = F_{du} \cos \theta_i \quad (8)$$

and

$$F_{duy} = F_{du} \sin \theta_i. \quad (9)$$

Bubble's growth depends on the temperature of the liquid surrounding the bubble. Zuber's bubble-growth model [18] agrees fairly well with flow boiling bubble-growth data in literature. Its equation is given as

$$r_b = \frac{2b}{\sqrt{\pi}} Ja \sqrt{\alpha_f t}, \quad (10)$$

where  $b$  is a constant suggested as 1.73 by Zeng et al. [7], and  $\alpha_f$  is the thermal diffusivity. The Jacob number is defined as

$$Ja = \frac{\rho_f C_{pf} \Delta T_{sat}}{\rho_g i_{fg}} = \frac{\rho_f C_{pf} (T_w - T_{sat})}{\rho_g i_{fg}}, \quad (11)$$

where  $C_{pf}$ ,  $\Delta T_{sat}$ ,  $i_{fg}$ ,  $T_w$  and  $T_{sat}$  are, respectively, the specific heat of liquid at constant pressure, the wall superheat, the latent heat, the wall temperature, and the saturation temperature.



For saturated boiling, the wall superheat can be used as the superheat in the Jacob number. However, for forced convection subcooled boiling, this becomes more complex. When a bubble is attached at the heater wall and the bubble size is small, the liquid surrounding the bubble is superheated and the bubble will grow. However, when the bubble grows to a certain size and the tip of the bubbles reaches the subcooled region, the bubble starts to collapse. The effective superheat surrounding the bubble would be less than the wall superheat [19]. Therefore, the bubble radius is a function of the effective Jacob number, Reynolds number, Prandtl number, and growth time  $t$  as

$$r = f(Ja_e, Re, Pr, t), \quad (12)$$

where the definition of  $Ja_e$  is

$$Ja_e = \frac{\rho_f C_{pf} \Delta T_e}{\rho_g i_{fg}}, \quad (13)$$

and

$$\Delta T_e = S(T_w - T_{sat}), \quad (14)$$

where  $S$  is the suppression factor.

**3.2.2.3. Shear lift force.** Saffman [20] derived the shear lift force on a solid sphere at low Reynolds number. Auton [21] derived an expression for the shear lift force on a sphere in an inviscid shear flow. Mei and Klausner [22] modified Saffman's model to suit for a bubble, and interpolated with Auton's equation to derive an expression for shear lift force over wide range of Reynolds number as

$$F_{sl} = \frac{1}{2} C_1 \rho_f \pi r_b^2 u_r^2, \quad (15)$$

where  $u_r$  is the relative velocity between the bubble center of mass and the liquid phase, i.e.,  $u_r = u_f - u_g$ , and the  $C_1$  is the shear lift coefficient given by [6]

$$C_1 = 3.877 G_s^{1/2} (Re_b^{-2} + 0.014 G_s^2)^{1/4}, \quad (16)$$

where

$$G_s = \left| \frac{du_f}{dx} \right| \frac{r_b}{u_r}, \quad (17)$$

and  $Re_b$  is the bubble Reynolds number

$$Re_b = \frac{2r_b u_r}{\nu_f}. \quad (18)$$

Fig. 8 shows the dependence of the shear lift coefficient on the bubble Reynolds number as a parameter of the non-dimensional liquid shear gradient,  $G_s$ . As shown in the figure, as the bubble Reynolds number increases, the shear lift coefficient approaches the Auton's lift coefficient.

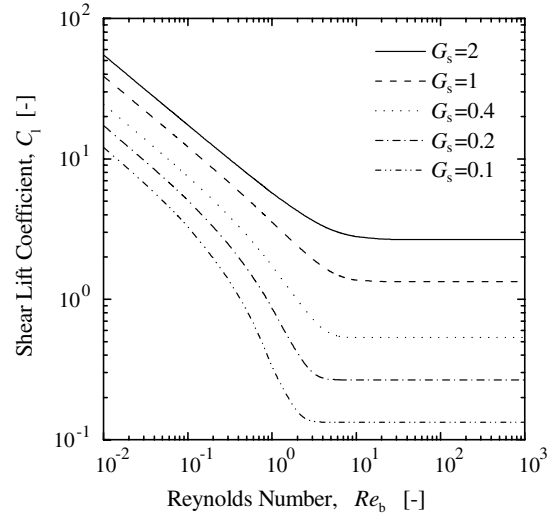


Fig. 8. Dependence of shear lift force coefficient on bubble Reynolds number.

The liquid velocity profile near the wall can be estimated by using universal single-phase turbulent flow profile. It is defined by

$$u^+ = \frac{1}{k^+} \ln x^+ + C^+, \quad (19)$$

where  $k^+$  and  $C^+$  are the constants depending on  $x^+$ , and

$$u^+ \equiv \frac{u_f}{u^*} = \frac{u_f}{\sqrt{\tau_w / \rho_f}}, \quad (20)$$

$$x^+ \equiv \frac{x u^*}{\nu_f} = \frac{x \sqrt{\tau_w / \rho_f}}{\nu_f}. \quad (21)$$

The dimensionless velocities for different regions are

$$\begin{cases} u^+ = x^+ & x^+ \leq 5, \\ u^+ = 5 \ln x^+ - 3.05 & 5 < x^+ < 30, \\ u^+ = 2.5 \ln x^+ + 5.5 & x^+ \geq 30. \end{cases} \quad (22)$$

The first equation in Eq. (22) is modified as

$$u^+ = \frac{4}{\ln 5} \ln x^+ + 1 \quad x^+ < 5. \quad (23)$$

The reason of this modification is to keep the same form in Eq. (19) for later derivation. The new equation equals to the equation  $u^+ = x^+$  when  $x^+$  is 1 or 5, and the difference in the range of  $1 < x^+ < 5$  is smaller than 14%. Experiments found that the bubble radii are in the range of  $x^+ > 1$ , thus this approximation is reasonable.

The wall shear stress  $\tau_w$  can be calculated by

$$\tau_w = C_f \cdot \frac{1}{2} \rho_f v_f^2, \quad (24)$$

where  $v_f$  is the area-averaged liquid velocity, and  $C_f$  is the friction coefficient as

$$C_f = \frac{\lambda}{4}, \tag{25}$$

where  $\lambda$  is the friction factor. For a smooth surface, the friction factor is expressed by

$$\begin{cases} \lambda = \frac{64}{Re} & Re < 2320, \\ \lambda = \frac{0.3164}{Re^{0.25}} & 4 \times 10^3 < Re < 10^5, \\ \lambda = 0.0032 + 0.221Re^{-0.237} & 10^5 < Re < 3 \times 10^6. \end{cases} \tag{26}$$

Here, Reynolds number,  $Re$ , is defined as  $Re = \rho_f v_f D_H / \mu_f$ , where  $D_H$  and  $\mu_f$  are the hydraulic equivalent diameter and the viscosity of liquid, respectively.

When a bubble is lift-off, the bubble may be sliding on the heating surface. However, no model or empirical correlation is found in literature to model the bubble sliding velocity. Thus, we define the relative velocity coefficient as

$$C_r \equiv u_r / u_f, \tag{27}$$

where  $u_f$  is the local liquid velocity at the bubble center of mass.  $C_r$  is unity when the bubble is not sliding, and it is zero when the bubble velocity is the same as the liquid velocity. Thus, the relative velocity coefficient is between 0 and 1 during the bubble lift-off process.

By implementing Eq. (19), one can derive the shear rate term in Eq. (17) as

$$\frac{du}{dx} = \frac{u^{*2}}{v_f} \frac{du^+}{dx^+} = \frac{u^{*2}}{v_f} \frac{1}{k^+ x^+} = \frac{u^*}{k^+ x^+}. \tag{28}$$

Thus Eq. (17) becomes

$$G_s = \left| \frac{du}{dx} \right|_{x=r_b} \frac{r_b}{u_r} = \left| \frac{u^*}{k^+ x} \right| \frac{r_b}{u_r} = \frac{1}{C_r k^+ u^+}. \tag{29}$$

**3.2.2.4. Pressure and gravity forces.** The pressure force on a bubble by the surrounding liquid is expressed as

$$F_p = \rho_f g V_b, \tag{30}$$

where  $V_b$  is the bubble volume. The gravity force can be obtained by

$$F_g = -\rho_g g V_b. \tag{31}$$

**3.2.2.5. Quasi-steady drag force.** For the quasi-steady drag force, Klausner et al. [6] modified the expression by Mei and Klausner [23] by taking into account the effect of the wall as

$$\frac{F_{qs}}{6\pi\rho_f v_f u_r r_b} = \frac{2}{3} + \left[ \left( \frac{12}{Re_b} \right)^n + 0.796^n \right]^{-1/n}, \tag{32}$$

where  $n = 0.65$ .

**3.2.3. Balance of forces acting on bubble at lift-off**

The force balance in  $x$ -direction at the moment of the bubble lift-off is shown in Fig. 9. The bubble surface tension force may be neglected at the bubble lift-off because the bubble contact area on the heater surface becomes zero at the moment of lift-off. Meanwhile, the bubble inclination angle is zero, thus the growth force becomes normal to flow direction. The force balance in  $x$ -direction results in

$$F_{du} + F_{sl} = 0. \tag{33}$$

Substituting the expressions of the growth force and shear lift force into Eq. (33) yields

$$-\rho_f \pi r_b^2 \left( \frac{11}{2} \dot{r}_b^2 + \frac{11}{6} r_b \ddot{r}_b \right) + \frac{1}{2} C_1 \rho_f \pi r_b^2 u_r^2 = 0. \tag{34}$$

Furthermore, substituting Eq. (10) into Eq. (34) yields

$$\frac{\alpha_f}{t_{lo}} = \frac{3\pi C_1 u_r^2}{22b^2 Ja^2}, \tag{35}$$

where  $t_{lo}$  is the time of lift-off. It can be derived from Eq. (10) as

$$t_{lo} = \frac{\pi r_{lo}^2}{4b^2 Ja^2 \alpha_f}. \tag{36}$$

By substituting Eq. (36) into Eq. (35), we can get

$$C_1 \left( \frac{u_r D_{lo}}{v_f} \right)^2 = \frac{352b^4}{3\pi^2} Ja^4 Pr_f^{-2}, \tag{37}$$

where  $Pr_f$  is the liquid Prandtl number,  $Pr_f = v_f / \alpha_f$ . A new dimensionless parameter of the bubble lift-off diameter is now defined by

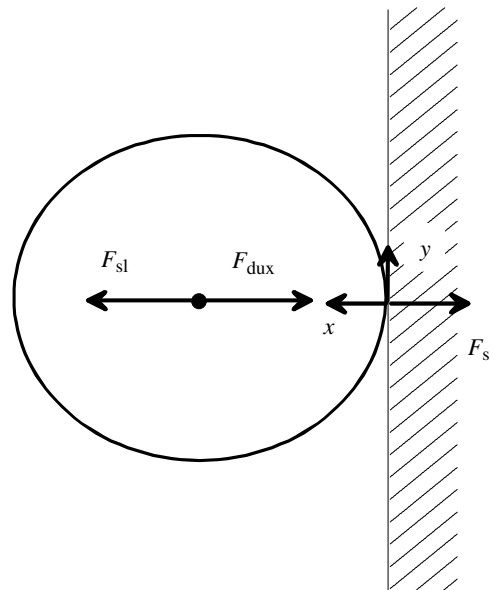


Fig. 9. Force balance of a vapor bubble at lift-off.

$$D_{lo}^* \equiv \sqrt{C_1} Re_b = \sqrt{C_1} \left( \frac{u_r D_{lo}}{\nu_f} \right). \quad (38)$$

The dimensionless bubble lift-off diameter is now a function of the Jacob number and the Prandtl number as

$$D_{lo}^* = \frac{4\sqrt{22/3}b^2}{\pi} Ja_c^2 Pr_f^{-1}. \quad (39)$$

In forced convective subcooled boiling flow, the effective wall superheat should be used for the Jacob number as discussed earlier. This yields

$$D_{lo}^* = \frac{4\sqrt{22/3}b^2}{\pi} Ja_c^2 Pr_f^{-1}. \quad (40)$$

### 3.3. Comparison of lift-off model with experimental data

In calculating the effective wall superheat based Jacob number,  $Ja_c$ , the wall temperature should be determined. No direct wall temperature measurement is available for the current water data. Therefore, the wall temperature needs to be calculated by using existing correlations or models.

In the present study, Sato and Matsumura's correlation (1964) (The original paper is not found, the correlation was cited by Davis and Anderson [24]) is used to calculate the onset of nucleation boiling (ONB)

$$q''_{ONB} = \frac{k_f i_{fg} \rho_v}{8\sigma T_{sat}} (T_w - T_{sat})^2, \quad (41)$$

where  $k_f$  is the thermal conductivity. Chen's correlation [25] is used to calculate the wall temperature in the subcooled boiling regions (modified by Collier [26])

$$q'' = h_{NB}(T_w - T_{sat}) + h_c(T_w - T_{bulk}), \quad (42)$$

where

$$h_c = 0.023 Re_f^{0.8} Pr_f^{0.4} \frac{k_f}{D_H} F, \quad (43)$$

where the factor  $F$  is set to unity and

$$h_{NB} = 0.00122 \left( \frac{k_f^{0.79} C_{pf}^{0.45} \rho_f^{0.49}}{\sigma^{0.5} \mu_f^{0.29} i_{fg}^{0.24} \rho_g^{0.24}} \right) \Delta T_{sat}^{0.24} \Delta \rho^{0.75} S, \quad (44)$$

where  $\mu_f$  is liquid dynamic viscosity,  $\Delta \rho$  is density difference between liquid and vapor phases, and

$$S = \frac{1}{1 + 2.53 \times 10^{-6} Re_{TP}^{1.17}}, \quad (45)$$

where  $Re_{TP}$  is the two-phase Reynolds number calculated by setting vapor quality as zero. Due to the short test section length and relatively small heater power available, the estimation of the point of net vapor generation does not considerably affect the calculation of the wall temperature.

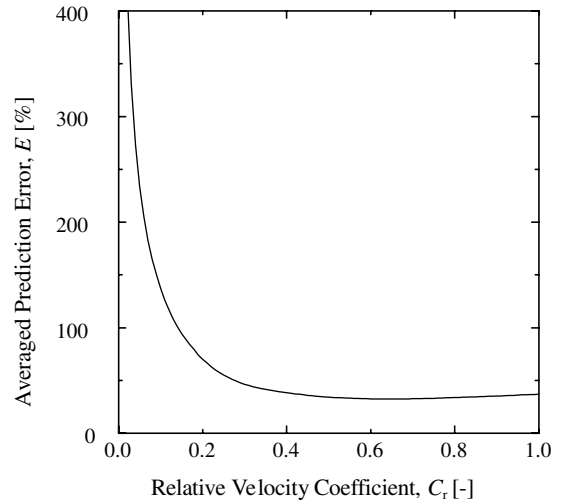


Fig. 10. Dependence of prediction error on relative velocity coefficient.

The effect of relative velocity coefficient is shown in Fig. 10. The averaged prediction error,  $E$ , is defined as

$$E \equiv \frac{|D_{lo,exp}^* - D_{lo,pred}^*|}{D_{lo,exp}^*} \times 100. \quad (46)$$

The figure indicated that the averaged prediction errors of the dimensionless bubble lift-off diameter are nearly constant below 40% when  $C_r$  is between 0.4 and 1. Since no model of the bubble sliding velocity exists, we assume the bubble sliding velocity is half of the local liquid velocity, i.e.,  $C_r = 0.50$ . The comparison of the model prediction and the current experimental data is shown in Fig. 11. The figure suggests that the data trend agrees well with the prediction. The average prediction error is  $\pm 35.2\%$ . No other bubble lift-off diameter data for upward flow is founded in literature. Extensive data of bubble lift-off diameter on various working fluids should be taken to evaluate the model in a future study. Special attention should be paid to the relative velocity coefficient  $C_r$ . In a future study, the sliding velocity may be studied on both experimental and theoretical aspects: In the experimental aspect, the bubble sliding velocity can be measured by analyzing the consecutive bubble sliding images. Further study may be performed to measure bubble sliding velocity in the present data and other data. On the other hand, at the theoretical aspect, the bubble sliding velocity may be able to calculate by assuming force balance along the flow direction. Recently, Sateesh et al. [27] calculated the sliding velocity along horizontal tube surface. It might be a promising approach. For horizontal flow, the buoyancy force should be considered in analyzing force balance. Zeng et al. [7] have 38 data sets of R113 in horizontal flow.

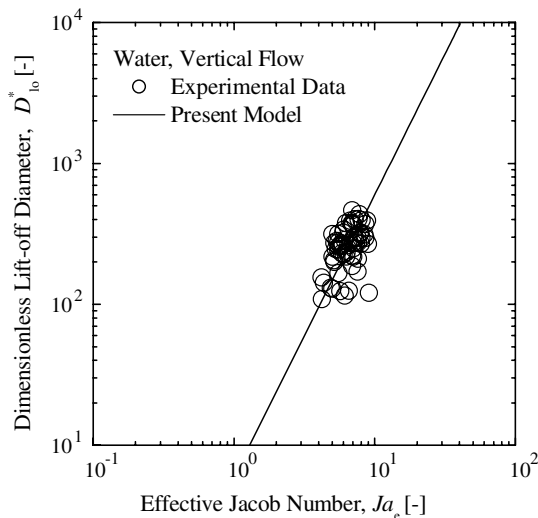


Fig. 11. Comparison between predicted and measured bubble lift-off diameters.

Using the expression of pressure and gravity force, Eqs. (28) and (29), the bubble lift-off diameter can be calculated. The comparison between calculated bubble lift-off diameter and experimental data shows the average prediction error is  $\pm 48.8\%$ . This suggests that the expressions of growth force and shear lift force are reasonable.

#### 4. Conclusions

Forced convective subcooled flow boiling experiments were conducted in a BWR-scaled vertical-upward annular channel by using water as testing fluid. The test runs were performed at atmosphere pressure. The inlet temperature ranged from 80.0 to 98.5 °C; the inlet velocity varied from 0.487 to 0.939 m/s; and the heat flux changed from 60.7 to 206 kW/m<sup>2</sup>. A high-speed digital video camera was used to capture the dynamics of the subcooled nucleation process. Bubble lift-off diameters were obtained from the images for a total of 91 test conditions. The results indicated that bubble lift-off diameter increases with increasing of the inlet temperature, increasing of the heat flux, or decreasing of the inlet fluid velocity.

The forces acting on a growing bubble at the nucleation site were discussed. Force balance analysis showed that the bubble is governed by growth force and shear lift force at the instant of the lift-off. A dimensionless term of bubble lift-off diameter was found to be a function of Jacob number and Prandtl number. The proposed model and experimental data agreed reasonably well within the averaged relative deviation of  $\pm 35.2\%$ .

#### Acknowledgements

The research project was supported by the Tokyo Electric Power Company (TEPCO). The authors would like to express their sincere appreciation for the support from the TEPCO. They would also like to thank Dr. Ye Mi (Purdue University, USA, currently at En' Urga Inc, USA) for the development of the image processing program.

#### References

- [1] M. Ishii, *Thermo-Fluid Dynamics Theory and Two-Phase Flow*, Eyrolles, Paris, 1975.
- [2] G. Kocamustafaogullari, M. Ishii, Foundation of the interfacial area transport equation and its closure relations, *Int. J. Heat Mass Transfer* 38 (1995) 481–493.
- [3] N. Zuber, Hydrodynamic aspects of boiling heat transfer, US AEC Rep. AECU 4439, Tech. Inf. Serv. Oak Ridge, Tenn., 1959.
- [4] N. Zuber, Recent trends in boiling heat transfer research. Part I: Nucleate pool boiling, *Appl. Mech. Rev.* 17 (1964) 663–672.
- [5] S. Levy, Forced convection subcooled boiling—prediction of vapor volumetric fraction, *Int. J. Heat Mass Transfer* 10 (1967) 951–965.
- [6] J.F. Klausner, R. Mei, D.M. Bernhard, L.Z. Zeng, Vapor bubble departure in forced convection boiling, *Int. J. Heat Mass Transfer* 36 (1993) 651–662.
- [7] L.Z. Zeng, J.F. Klausner, D.M. Bernhard, R. Mei, A unified model for the prediction of bubble detachment diameters in boiling systems—II. Flow boiling, *Int. J. Heat Mass Transfer* 36 (1993) 2271–2279.
- [8] F.W. Staub, The void fraction in subcooled boiling—prediction of the initial point of net vapor generation, *J. Heat Transfer* (1968) 151–157.
- [9] R.A.M. Al-Hayes, R.H.S. Winterton, Bubble diameter of detachment in flowing liquids, *Int. J. Heat Mass Transfer* 24 (1981) 223–230.
- [10] J.T. Rogers, M. Salcudean, Z. Abdullah, D. McLeod, D. Poirier, The onset of significant void in up-flow boiling of water at low pressure and velocities, *Int. J. Heat Mass Transfer* 30 (1987) 2247–2260.
- [11] S.G. Kandlikar, B.J. Stumm, A control volume approach for investigating forces on a departing bubble under subcooled flow boiling, *Fundamentals of Phase Change: Boiling and Condensation ASME HTD-vol. 273* (1994) 73–80.
- [12] M. Bartel, M. Ishii, T. Masukawa, Y. Mi, R. Situ, Interfacial area measurements in subcooled flow boiling, *Nucl. Eng. Des.* 210 (2001) 135–155.
- [13] R. Situ, T. Hibiki, X. Sun, Y. Mi, M. Ishii, Flow structure of subcooled boiling flow in an internally heated annulus, *Int. J. Heat Mass Transfer* 47 (2004) 5351–5364.
- [14] R. Situ, T. Hibiki, X. Sun, Y. Mi, M. Ishii, Axial development of subcooled boiling flow in an internally heated annulus, *Exp. Fluids* 37 (2004) 589–603.
- [15] R. Situ, Y. Mi, M. Ishii, M. Mori, Photographic study of bubble behaviors in forced convection subcooled boiling, *Int. J. Heat Mass Transfer* 47 (2004) 3659–3667.

- [16] T. Hazuku, N. Tamura, N. Fukamachi, T. Takamasa, T. Hibiki, M. Ishii, Axial development of vertical upward bubbly flow in a minipipe, in: Proceedings of HT2005, 2005 ASME Summer Heat Transfer Conference, San Francisco, CA, USA, July 17–22, 2005.
- [17] Y. Chen, M. Groll, R. Mertz, R. Kulenovic, Force analysis for isolated bubbles growing from smooth and evaporator tubes, *Trans. Inst. Fluid-Flow Mach.* 112 (2003) 57–74.
- [18] N. Zuber, The dynamics of vapor bubbles in nonuniform temperature fields, *Int. J. Heat Mass Transfer* 2 (1961) 83–98.
- [19] G. Kocamustafaogullari, M. Ishii, Interfacial area and nucleation site density in boiling systems, *Int. J. Heat Mass Transfer* 26 (1983) 1377–1387.
- [20] P.G. Saffman, The lift on a small sphere in a slow shear flow, *J. Fluid Mech.* 22 (1965) 385–400.
- [21] T.R. Auton, The lift force on a spherical body in a rotational flow, *J. Fluid Mech.* 183 (1987) 199–218.
- [22] R. Mei, J.F. Klausner, Shear lift force on spherical bubbles, *Int. J. Heat Fluid Flow* 15 (1994) 62–65.
- [23] R. Mei, J.F. Klausner, Unsteady force on a spherical bubble at finite Reynolds number with small fluctuations in the free-stream velocity, *Phys. Fluids A* 4 (1992) 63–70.
- [24] E.J. Davis, G.H. Anderson, The incipience of nucleate boiling in forced convection flow, *AIChE J.* 12 (1966) 774–780.
- [25] J.C. Chen, Correlation for boiling heat transfer to saturated fluids in convective flow, *Ind. Eng. Chem. Proc. Des. Devel.* 5 (1966) 322–329.
- [26] J.G. Collier, Heat transfer in the post dryout region and during quenching and reflooding, in: G. Hetsroni (Ed.), *Handbook of Multiphase Systems*, Hemisphere, New York, 1982.
- [27] G. Sateesh, S.K. Das, Ar.R. Balakrishnan, Analysis of pool boiling heat transfer: effect of bubbles sliding on the heating surface, *Int. J. Heat Mass Transfer* 48 (2005) 1543–1553.